Evaluation of the simulated interannual and subseasonal variability in an AMIP-style simulation using the CSU Multi-scale Modeling Framework

Marat Khairoutdinov[1] and David Randall

Department of Atmospheric Science
Colorado State University

Submitted to
Journal of Climate

August 2006

[1] Corresponding author address: Marat Khairoutdinov, Department of Atmospheric Science, Colorado State University, Fort Collins, CO 80523 e-mail: marat@atmos.colostate.edu

Abstract

The Colorado State University (CSU) Multi-scale Modeling Framework (MMF) is a new type of global climate model (GCM) that replaces the conventional parameterizations of convection, clouds and boundary layer with a cloud-resolving model embedded into each grid column. The MMF has been used to perform a 19-year long AMIP style simulation using the 1985-2004 sea surface temperature (SST) and sea ice distributions as prescribed boundary conditions. Particular focus has been given to the simulation of the interannual and subseasonal variability.

The annual mean climatology is generally well simulated. Prominent biases include excessive precipitation associated with the Indian and Asian Monsoon seasons, precipitation deficits west of the Maritime Continent and over Amazonia, shortwave cloud effect biases west of the subtropical continents due to insufficient stratocumulus clouds, and longwave cloud effect biases due to overestimation of high cloud amounts especially in the Tropics. The geographical pattern of the seasonal cycle of precipitation is well reproduced, although the seasonal variance is considerably overestimated mostly because of the excessive monsoon precipitation mentioned above. The MMF does a good job of reproducing the interannual variability in terms of spatial structure and magnitude of major anomalies associated with the the El Niño / Southern Oscillation (ENSO). The simulations of the subseasonal variability of tropical climate associated with the Madden-Julian Oscillation (MJO) and equatorially trapped waves are particular strengths of the simulation. The wavenumber-frequency power spectra of the simulated outgoing longwave radiation (OLR) for time scales in the range 2 to 96 days compare very well to the spectra derived from observations, and show a robust MJO, Kelvin waves and Rossby waves with phase speeds similar to those observed. The

geographical patterns of the MJO and Kelvin-wave filtered OLR variance for summer and winter seasons are well simulated, but the variances are overestimated by as much as 50%. The observed seasonal and interannual variations of the strength of the MJO are also well reproduced.

1. Introduction

In a new type of general circulation model (GCM), many processes that unresolved on GCM grid are incorporated using a cloud-resolving model (CRM; Grabowski and Smolarkiewicz 1999; Grabowski 2001; Khairoutdinov and Randall 2001; Khairoutdinov et al.2005). The CRM, which in this context is often call super-parameterization, is inserted into each GCM grid column. From the GCM's prospective, the CRM works like a set of conventional parameterizations. The CRM is forced by the GCM-grid scale tendencies, and the CRM generates vertical profiles of tendencies. Such a 'super-parameterized' GCM has been termed a Multi-scale Modeling Framework, or MMF. This name emphasises that such a model includes in a single framework not only the scales of atmospheric motion on the order of hundreds kilometers as represented on the GCM's grid, but also the meso-scale and cloud-scale circulations that are represented on the CRM's grid. In this sense, MMF is regarded as a bridge between the conventional GCMs and the immensely more computationally expensive global CRMs that have just recently been applied for short global simulations (Tomita et al. 2005; Miura et al. 2005).

A major strength of the MMF concept is that it allows cloud microphysics, aerosols, turbulence, and radiation interact on the *cloud*-scale, as they do in nature. In contrast, various parameterizations of unresolved physical processes in conventional GCMs do not generally communicate directly with each other but rather through modification of the scales that are represented on the GCM's coarse grid, which are generally much larger than the cloud scale. Recent experiments with the MMF has indicated that such cloud-scale interactions ignored in conventional GCMs can be quite important. For example, Khairoutdinov et al. (2005) has shown that the MMF tends to improve the diurnal cycle of precipitation over summertime

continents quite dramatically when compared to the conventional version of the same GCM. Cole et al.(2005) has demonstrated the importance of cloud-scale interactions between clouds and radiation for the simulated global distribution of clouds and radiation. The problem of the scale of interactions represents just one of many other problems associated with the current state of the art of the physical parameterizations, and the MMF approach is argued to be one of the plausible pathways to the future (Randall et al. 2003; Arakawa 2004).

The MMF has a substantially higher computational cost than a conventional GCM. For example, when run on the *same* number of CPUs in our first MMF experiments (Khairoutdinov and Randall 2001), the CSU MMF was about two orders of magnitude slower than the host GCM with conventional parameterizations. However, since the ratio of the time that that MMF spends computing to the time spent for inter-CPU communication is much higher than the same ratio for conventional GCMs, the MMF can be vastly more scalable on parallel computers, i.e., it can utilize large number of CPUs more efficiently than conventional GCMs. For example, the CSU MMF results presented in this paper were obtained using 1024 CPUs of the "Seaborg" supercomputer at NERSC[2] with more than 90% parallel efficiency (see Fig. 2 of Khairoutdinov et al. 2005). As a result, it currently takes roughly one wall-clock day (on Seaborg) to simulate one year on a 2.8^ox2.8^o horizontal grid (T42 spectral truncation) with 30 vertical levels. Such performance is about 20 times better in terms of the wall-clock time performance than it was in our first MMF experiments using similar processors.

It is expected that, over the next decade, the computational performance of the CSU MMF will improve further on the faster systems of the future, so that century-long climate-change

[2] The Department of Energy's National Energy Research Scientific Computing Center

simulations using a coupled atmosphere-ocean MMF model may become feasible. Even now, it is feasible to make runs as long as a decade. For example, the CSU MMF was recently used to conduct a relatively simple Cess-type climate sensitivity experiment (Cess et al. 1996). The results were reported by Wyant et al. (2006). A multi-year control simulation was compared to an experiment in which the prescribed climatological sea-surface temperature (SST) was uniformly increased by 2 K.

It has also become feasible to use the MMF in AMIP[3]-style simulations based on prescribed observed monthly-mean SSTs and sea-ice cover, for a period of more than a decade. Recently, short AMIP-style MMF simulations using the 1998-1999 observed SSTs were conducted at Pacific Northwest National Laboratory (Ovtchinnikov et al. 2006) with a version of MMF similar to the CSU MMF, and also at NASA Goddard Space Flight Center (Tao et al. 2006) using a completely different MMF.

In this paper, we present the results of the first decadal AMIP-style simulation with the CSU MMF using the 1985-2004 observed SSTs. The emphasis of our analysis is on the simulated subseasonal and interannual variability as compared to observations.

[3] Atmospheric Model Intercomparison Project
[6] National Center for Atmospheric Research

2. Simulation setup

The CSU MMF was described in detail by Khairoutdinov at al. (2005; hereinafter referred to as K05). The host GCM is the NCAR[6] Community Atmosphere Model (CAM), version 3, which is the atmospheric component of the NCAR Community Climate System Model (CCSM; Collins et al.2006). We use a semi-Lagrangian dynamical core as it allows us to achieve better scalability of the MMF when using large number of processors. The dynamical core was configured to run with 2.8^o x 2.8^o horizontal grid spacing (T42 truncation) with 30 levels, and the domain top at 3.6 hPa. The GCM timestep was 30 min. In each grid column, all of the conventional moist physics, convective, turbulence and boundary-layer parameterizations, except for the gravity-wave drag parameterization, were replaced by a CRM, which is a two-dimensional version of the System for Atmospheric Modeling (SAM; Khairoutdinov and Randall, 2003).

The CRM solves the momentum equations using the anelastic approximation. The prognostic thermodynamic variables include the liqui/ice water moist static energy, total precipitating and total non-precipitating water. Cloud condensate is diagnosed using the 'all-or-nothing' condensation scheme assuming saturation with respect to water/ice. Precipitating water is a mixture of the snow, graupel and rain water with the hydrometeor partitioning assumed to be a function of temperature only. The precipitation sources and sinks are computed using a simple bulk microphysics model.

In this study, the CRM's two-dimensional domain had 32 grid columns with 4-km horizontal grid spacing, and 28 layers collocated with the GCM grid layers. The timestep was 20 sec. The domain was periodic and aligned in the south-north direction; this is different from K05, who used the east-west alignment. The motivation for this change is that it seems

to mitigate the positive precipitation bias in the Western Pacific for the summer months (K05).

The subgrid-scale fluxes were computed using the first-order turbulent closure based on the Smagorinski model for the eddy diffusivity and viscosity. The CAM radiative transfer scheme was applied every 15 min for each CRM column using the all-or-nothing cloud overlap assumption.

During the GCM timestep, the CRM was forced by the large-scale tendencies arising from GCM dynamical processes. The forcing was applied uniformly in the horizontal, and computed as described in K05. The CRM output consisted of horizontally averaged tendencies of temperature, water vapor and cloud condensate, which were used to feed back on the GCM fields. The GCM's horizontal wind was not modified by the CRM because of concern that the vertical momentum transport simulated by the two-dimensional model is unrealistic. Instead, the conventional parameterizations of the host GCM were allowed to alter the wind field (see the discussion and experiments reported by K05). The surface fluxes were computed on the GCM grid with a local gustiness enhancement of the surface stress on the CRM grid.

The AMIP-style integration presented in this study was performed using prescribed monthly-mean SST and sea ice datasets provided by J. Hurrell of NCAR. The integration period was from September 1, 1985 to September 1, 2004, i.e., a total of simulated 19 years. The monthly and yearly means were computed for 1986 through 2003.

3. Results

a. Simulated annual-mean climatology

The global distribution of annual mean precipitation for the MMF is shown in Fig. 1, along with the observed CMAP[7] climatology (Xie and Arkin 1997) and the corresponding mean error for years 1986-2001. The overall pattern of precipitation is generally well reproduced; but, there are important deficiencies. The most prominent are the deficits of precipitation in the Indian Ocean just to the west of the Maritime Continent, in the western Pacific intertropical convergence zone (ITCZ), south Atlantic storm trek, and over the Amazonia. Most notable precipitation regions of excessive simulated precipitation are in the northwest tropical Pacific during the South Asian Monsoon season, and in the western India and Bay of Bengal during the Indian Monsoon season. Also, there is a `bull's eye` of excessive precipitation in equatorial South America. The positive monsoon season biases have also been evident in earlier MMF simulations with prescribed climatological SSTs (Khairoutdinov et al. 2005). There is a clear underestimation of precipitation in the region where the ITCZ and the South Pacific convergence zone merge, and an overestimation just south of the equator; this is a manifestation of the double-ITCZ problem.

Precipitation in Africa and Eurasia is generally well simulated, while considerable biases are present in North and South America. The global-mean annual precipitation is overestimated by about 0.14 mm/day with respect to the CMAP estimate of 2.66 mm/day (Table 1).

[7] Climate Prediction Center Merge Analysis of Precipitation

The geographical distribution of the annually averaged column integrated water vapor, or precipitable water, and its difference from the NVAP (Randel et al., 1996) climatology, is shown in Fig. 2. Although the MMF captures the observed patterns quite well, there are considerable biases. Precipitable water is systematically overestimated over most of the oceans with the most prominent error in the equatorial eastern Pacific. The most notable maritime negative biases are in and around the Maritime Continent and equatorial Atlantic. Over land, the simulation is systematically too dry over the subtropical continents, and too wet over central Africa, suggesting that the simulated Hadley circulation is stronger than in nature. There is a clear tendency for unrealistically dry air over the maritime regions west off the subtropical continents, where stratocumulus clouds are observed to form. This contributes to an underestimation of low-level clouds in those regions. The globally average precipitable water is overestimated by 0.7 mm (Table 1).

The global distributions of the annual mean longwave (LWCE) and shortwave (SWCE) cloud effects are shown in Fig. 3 and Fig. 4, respectively, along with the observational estimates from the ISCCP-FD data set (Zhang et al. 2004) and the mean error distribution for years 1986-2000. The cloud effect is the difference between the clear-sky and total fluxes at the top-of-atmosphere (TOA), and, thus, is a direct measure of the cloud effect on the TOA radiation. The global annual mean values for MMF match the observational estimates rather well (Table 1). The TOA global annual mean fluxes have been tuned[8] to force the net radiation be close to zero; however, the global mean SWCE and LWCE have not been intentionally tuned, but their good match with observational estimates appears to be a result of cancellation of rather large regional biases. The geographical distribution of LWCE biases

[8] Shortwave radiation was tuned by a slight reduction of the specified liquid water drop effective radius relative to the standard CAM. Longwave radiation was not tuned.

generally resembles the precipitation biases, which is expected since the outgoing longwave radiation is mostly affected by deep precipitating. Therefore, we expect that improvements in the global distribution of precipitation will lead to a general improvement in the geographical pattern of longwave radiation.

The large negative biases in the SWCF (Fig. 4) are also well correlated with the positive precipitation biases due to the fact that more active deep convection and, as the result, more extensive anvils in the model tend to reflect more sunlight back to space. The global high-cloud cover is slightly overestimated by the MMF (Table 1). The largest positive SWCE biases are, not surprisingly, situated to the west from the subtropical continents, where the stratocumulus clouds are observed. The MMF consistently underestimates the occurrence of low-level clouds such as trade cumuli and stratocumuli, because of the coarse resolution of the super-parameterization's grid. Although there are low-level clouds in the MMF and their spatial distribution is somewhat realistic their amount is underestimated, especially in the subtropics (not shown). Further discussion is given by K05.

The net shortwave radiation absorbed by the surface is underestimated by about 7 W m^{-2} compared to the ISCCP-FD estimates (Table 1) with much smaller bias under clear skies. Net surface longwave flux is overestimated also by 7 W m^{-2}, with a comparable bias under clear skies. Despite the biases in the surface radiation budget, the global mean turbulent surface fluxes are within 3 W m^{-2} of the Kiehl and Trenberth (1997) estimates; however, the estimates themselves are subject to significant uncertainties. The MMF simulation has biases in the zonal structure of the temperature field (not shown) similar to those seen in the earlier climatological SST run (see Fig. 12 of K05), with a significant cold bias in the temperature of the tropical tropopause.

b. Seasonal variability

The seasonal cycle is a major forced mode of climate variability. One of many ways to evaluate the simulated mean seasonal cycle is to look at the geographical distribution of the amplitude and phase of the first annual harmonic, for various variables. Fig. 5 shows the first annual harmonic of the precipitation rate, from the MMF simulation and from CMAP. The monthly mean precipitation for the period 1986-2003 was used to define a mean annual cycle. In general, the simulated and observed patterns of the seasonal variation amplitude are quite similar. The most notable overestimation of the seasonal precipitation amplitude is in the Indian and Asian monsoon regions, which is consistent with the large biases of the mean precipitation there (see Fig. 1). The geographical pattern of the average month of the precipitation maximum as seen in the first annual harmonic closely resembles the observed pattern. There are biases in North America and Europe, where the simulated phase is about two months ahead of the observations.

In the CMAP monthly data, the first annual harmonic of the precipitation rate explains 41% and 34% of the total precipitation variance in the Tropics and midlatitudes[9], respectively. The corresponding values from the MMF are 33% and 27%, respectively These underestimates are mostly due to *overestimates* of the total variance of monthly precipitation for the whole AMIP run, by a factor of 1.83 for the tropics and 1.57 for midlatitudes. The ratios of the simulated to observed annual-harmonic's variance in the tropics and midlatitudes, are 1.48 and 1.24, respectively. These numbers also indicate that most of the overestimation

[9] Here the tropics are defined as the belt from 30^{o}S to 30^{o}N , and the midlatitudes between 30^{o} and 60^{o} in both hemispheres. The contribution of each grid cell was weighted by its surface area.

of variability of precipitation in tropics is due to an unrealistically strong annual cycle associated with the Indian and Asian monsoon biases discussed earlier.

c. Interannual variability

The El Niño / Southern Oscillation (ENSO) is the most important mode of interannual variability on sub-decadal scales, especially in the tropics. In this study of uncoupled integrations, only the forced atmospheric response to evolving but prescribed SST anomalies can be examined and compared to observations. Two analysis methods have been used: empirical orthogonal function (EOF) analysis and simple compositing. To reveal the structure of the interannual variations, EOF analysis was applied to the bandpass-filtered monthly data, i.e., with the annual cycle and shorter time-scales removed. In Fig. 6, the results for the precipitation rate anomalies are compared to observations for the first and second EOFs, denoted by EOF1 and EOF2. The MMF simulation does a very good job in reproducing the spatial patterns of both modes. The simulated EOF1 explains 19% of the variance, with EOF2 explaining about half of that. This is a similar to what is observed, except that in observations EOF1 explains up to a third of the variance. The observed time series of principle components (PCs) of the two modes are well reproduced by the MMF, especially for the leading mode. The peaks of the PC1 time series correspond to the El Niño events, while the troughs mark the La Niña events.

Another simple way of looking at the response of the atmosphere to the ENSO SST anomalies is to look at the spatial pattern of the differences between the annually averaged anomalies for a composite El Niño year and composite La Niña year. The contributing years have been selected based on the observed PC1 for the precipitation rate, and the number of

years for a given field was limited by the availability of observational estimates for a given ENSO phase. The same years were used for the MMF results and observations. Figure 7 shows the composite anomalies for several fields. As was the case with the precipitation anomaly, the MMF does a good job of reproducing the spatial structure and shape as well as magnitude of major positive and negative anomalies. There are some discrepancies with respect to observations for the weaker anomalies, especially over the continents; however, the statistical significance of those differences is hard to access without running a multi-member ensemble of MMF simulations, which is not currently practical.

d. Subseasonal variability in the tropics

While the variability of simulated atmosphere associated with the ENSO in the AMIP-style simulation is essentially forced by the imposed SST anomalies, the subseasonal variability for time scales of 100 days or shorter is mostly due to internal modes. Here we examine the ability of the MMF to simulate the tropical subseasonal variability associated with convectively coupled equatorial waves such as Kelvin and equatorial Rossby waves, as well as, of course, the Madden-Julian Oscillation (MJO; Madden and Julian 1972). The MJO is a major mode of subseasonal variability in the tropics, and is equally important for both climate and weather prediction. MJO has teleconnections with the extratropics and is believed to play important role in triggering El Niño events. Unfortunately, subseasonal variability, and especially the MJO, is generally very poorly simulated by most contemporary GCMs (e.g., Lin et al., 2006).

In our earlier experiments with climatological SSTs (Randall et al.2003; Khairoutdinov et al.2005), the MMF simulations showed a robust MJO with a realistic structure. Although quite encouraging, those early experiments were relatively short, each about year and half, with just a few MJO events. In this study, we compared the MJO statistics as simulated by the MMF over 18-year period with statistics derived from the similarly lengthy observations. The longer records make the comparison more robust.

It has become a rather standard approach to look at the dominant subseasonal modes of variability using the methods of Wheeler and Kiladis (1999; hereafter WK) who analyzed the wavenumber-frequency spectrum using the ratio of the raw spectral power to the power of a "background spectrum," which is simply a sufficiently smoothed raw spectrum. The WK procedure was applied to daily mean data from the MMF and from observations. To reduce the noise, the data was divided into 96-day-long segments overlapping each other by 60 days. Thus, the lowest resolved frequency was 1/96 cycle per day, while the highest frequency was 1/2 cycle per day. We looked only at the equatorially trapped waves, so only the data in the 15^{o}S-15^{o}N latitudinal belt were considered. For each analyzed field, two sets of wavenumber-frequency spectra were calculated, one for the symmetric and one for the antisymmetric components about the equator. Here we present the symmetric spectra only because they contain most of the power.

Figure 8 shows the WK diagram for the outgoing longwave radiation (OLR) for the MMF and for the standard CAM3 AMIP-style run (case eul64x128_d50amip), along with the corresponding results from the 1979-2004 daily NOAA AVHRR interpolated OLR data (Liebmann and Smith 1996). Positive zonal wavenumbers indicate eastward propagating disturbances; the lines in the figure are the theoretical dispersion curves for the shallow-water

equations for selected equivalent depths. In the observations, one can clearly see that the MJO occupies the spectral window of eastward wavenumbers of 1-4 and periods of about 50 to 100 days. The eastward moving Kelvin waves and westward moving Rossby waves follow the theoretical dispersion curves corresponding to a 25-m equivalent depth. All three of these modes are captured quite well by the MMF. The Kelvin wave is a bit weak but appears to propagate at about observed speed. In contrast, the simulation produced with the standard CAM3 lacks most of the MJO power, and although the Kelvin wave has a strong amplitude its phase speed is too fast, corresponding to an equivalent depth of more than 50 m.

The wavenumber-frequency spectra can be filtered to extract the signal associated only with particular disturbances of interest by zeroing the spectrum except for the spectral region that contains the selected modes. The corresponding space-time structures of the selected modes can then be generated from the filtered spectra using the inverse complex FFT. [10] The results of such filtering for the MMF simulation are illustrated by Fig. 9 which shows the Hovmuller diagrams for the MJO, Kelvin and equatorial Rossby wave filtered OLR as well as for the full or unfiltered OLR anomalies.

Figure 10 shows the geographical distribution for the simulated and observed OLR variance of the disturbances associated with the MJO averaged for the boreal winter, boreal summer, and the annual average. Overall, the pattern of OLR variability is well reproduced by the MMF. As in the observations, the simulated MJO is mostly confined to the Indian ocean and the western Pacific. Also, the MJO is considerably stronger during the boreal winter, with

[10] Strictly speaking, the new data set will also contain also some random noise contributed from the background spectrum at the same frequencies and wavenumbers as the desired disturbance. The amplitude of that noise will be much smaller though than the amplitude of the disturbance if the signal-to-noise ratio for that disturbance power spectrum is sufficiently larger than one which is the case for the MJO, Kelvin, and Rossby waves.

the maximum activity just north from Australia, as observed. During boreal summer, the MJO can propagate much further eastward, just north from the equator, all the way to the Gulf of Mexico. This is also well captured by the MMF. However, the magnitude of the OLR variance is overestimated by about 50% (please note that different color bars are used for the MMF and observations). Unlike most of GCMs which typically produces an MJO which is too weak, the MMF tends to make the MJO stronger than observed. As discussed by K05, experiments with convective momentum transport (using a version of the MMF that has a three-dimensional CRM) produce a slightly weaker, more realistic MJO.

Figure 11 compares the simulated and observed geographical distribution of variance associated with Kelvin wave. As was the case with the MJO, the MMF does very good job in reproducing the Kelvin wave variance spatial pattern, as well as the seasonal variations; however, the magnitude of the variance is again overestimated.

To examine the seasonal and interannual variability of the MJO, one can plot the mean MJO filtered OLR variance for each of the overlapping 96-day data segments against the time at the middle of the segment. This is shown in Fig. 12 along with the corresponding plot based on the NOAA OLR. Note that the multiyear mean variance was subtracted from both time series to accentuate the periods with below-average OLR anomalies, or weak MJO. In the MJO simulation, the periods with the strongest MJO events tend to occur during boreal winter, in agreement with observations. The strength of the simulated MJO varies quite a bit from year to year. This is also seen in the observations.

4. **Conclusions and future plans**

A Multi-scale Modeling Framework, or MMF, is a climate model in which all of the conventional parameterizations of clouds and the boundary layer are replaced with a cloud-resolving model that explicitly represents the bulk of the dynamical processes that are unresoved by the GCM. The first two-month integration using such a framework was presented in 2001. Since then, the results of a set of relatively short simulations have been reported in several publications that examined the aspects of mean seasonal climatology and subseasonal variability, climate sensitivity, the effects of radiation-cloud interactions, domain dimensionality, among others. In the present study, we present preliminary results from a 19-year long AMIP-style simulation in which the MMF is forced with prescribed SSTs and sea ice from September 1985 to September 2004. Such a prolonged simulation makes it possible to assess the ability of the MMF to simulated the interannual, seasonal, and, subseasonal variability of the present climate. The observed changes in the atmospheric hydrological cycle and the TOA radiation fields, in response to the interannual variability of the SST, are generally well reproduced by the MMF, as is the seasonal cycle. The subseasonal variability associated with the MJO and equatorially trapped waves is an area where MMF is particularly successful. An area of concern is overprediction by as much as 50% of the MJO-related variance of the outgoing longwave radiation. The seasonality of the MJO and its large interannual variability are quite realistically simulated by the MMF.

Many aspects of the simulated mean multiyear climatology are quite familiar from our earlier experiments with prescribed climatological SST, such as persistent precipitation excesses in the Indian and Asian Monsoon regions, large positive biases in the shortwave cloud effect due to a lack of stratocumulus and other low-level clouds, and an excessively

cold tropical tropopause. Many of the biases associated with the hydrological cycle may be related to of the parameterized microphysics in the cloud-resolving model, particularly the ice microphysics. Therefore, further refinement of the microphysics may lead to improvements in the performance of the model. The TOA flux biases associated with underprediction of the low-level clouds, including trade cumulus and stratocumulus clouds, are not as straightforward to alleviate. A simple increase of the grid resolution is currently not a viable option due to dramatic increase of already high computational cost of running MMF. Several possible pathways of addressing this problem without prohibitive cost increase are currently being tested.

Acknowledgments

Computing resources were provided by the Department of Energy's National Energy Research Scientific Computing Center (NERSC). This research was supported by the U.S. Department of Energy Grant DE-FG02-02ER63370 to Colorado State University as part of the Atmospheric Radiation Measurement Program.

References

Arakawa, A., 2004: The Cumulus Parameterization Problem: Past, Present, and Future. *J. Climate*, **17**, 2493-2525.

Cess, R. D., 1996: Cloud feedback in atmospheric general circulation models: An update. *J. Geophys. Res*., **101**, 12791-12794.

Cole J. N. S., H. W. Barker, D. A. Randall, M. F. Khairoutdinov, and E. E. Clothiaux, 2005: Global consequences of interactions between clouds and radiation at scales unresolved by global climate models. *Geophys. Res. Lett*., **32**, L06703.

Collins, W. D., and others, 2006: The Community Climate System Model version 3 (CCSM3*). J. Climate*, **19**, 2122-2143.

Grabowski, W. W., and P. K. Smolarkiewicz, 1999: CRCP: A cloud resolving convective parameterization for modeling the tropical convective atmosphere. *Physica D*, **133**, 171-178.

Grabowski, W. W., 2001: Coupling Cloud Processes with the Large-Scale Dynamics Using the Cloud-Resolving Convection Parameterization (CRCP). *J. Atmos. Sci.*, **58**, 978–997.

Khairoutdinov, M. F., and D. A. Randall, 2001: A cloud resolving model as a cloud parameterization in the NCAR Community Climate System Model: Preliminary results.

Geophys. Res. Lett., **28**, 3617–3620.

Khairoutdinov, M. F., and D. A. Randall, 2003: Cloud resolving modeling of the ARM summer 1997 IOP: Model formulation, results, uncertainties and sensitivities. *J. Atmos. Sci.*, **60**, 607-625.

Khairoutdinov, M.F., D.A. Randall, and C. DeMotte, 2005: Simulations of the atmospheric general circulation using a cloud-resolving model as a super-parameterization of physical processes. *J. Atmos. Sci*., **62**, 2136-2154.

Kiehl, J. T., and K. E. Trenberth, 1997: Earth's annual global mean energy budget. *Bull. Amer. Meteor. Soc*., **78**, 197-208.

Li, J.-L., and 15 others, 2005: Comparisons of EOS MLS cloud ice measurements with ECMWF analyses and GCM simulations: Initial results. *Geophys. Res. Lett*., **32**, L18710.

Liebmann, B, and C. A. Smith, 1996: Description of a complete (interpolated) outgoing longwave radiation dataset. *Bull. Amer. Meteor. Soc*., **77**, 1275-1277.

Lin, J.-L., and 15 others, 2006: Tropical intraseasonal variability in 14 IPCC AR4 climate models. Part I: Convective signals. *J. Climate*, **19**, 2665-2690.

Madden, R. A., and P. R. Julian, 1972: Description of global-scale circulation cells in the

tropics with 40-50 day period. *J. Atmos. Sci*., **29**, 1109-1123.

Miura, H., H. Tomita, T. Nasuno, S. Iga, M. Satoh, and T. Matsuno, 2005: A climate sensitivity test using a global cloud resolving model under an aqua planet condition. *Geophys. Res. Lett*., **32**, L19717.

Ovtchinnikov, M., T. P. Ackerman, R. T. Marchand, and M. F. Khairoutdinov, 2006. Evaluation of the Multi-scale Modeling Framework Using Data from the Atmospheric Radiation Measurement Program. *J. Climate*, **19**, 1716-1729.

Randall, D. A., M. Khairoutdinov, A. Arakawa, and W. Grabowski, 2003: Breaking the cloud-parameterization deadlock. *Bull. Amer. Meteor. Soc*., 84, 1547-1564.

Randel, D. L., and Coauthors, 1996: A new global water vapor dataset. *Bull. Amer. Meteor. Soc*., **77**, 1233-1246.

Tao, W.-K., and 8 others: Multi-scale Modeling System: Developments, applications, and critical issues. In preparation.

Tomita, H., H. Miura, S. Iga, T. Nasuno, and M. Satoh, 2005: A global cloud-resolving simulation: Preliminary results from an aqua planet experiment. *Geophys. Res. Lett*., **32**, L08805.

Wheeler, M., and G. N. Kiladis, 1999: Convectively coupled equatorial waves: Analysis of

clouds and temperature in the wavenumber-frequency domain. *J. Atmos. Sci*., **56**, 374-399.

Wyant, M. C., M. Khairoutdinov, and C. S. Bretherton, 2006: Climate sensitivity and cloud response of a GCM with a superparameterization. *Geophys. Res. Lett*., **33**, L06714.

Xie, P., and P. A. Arkin, 1997: Global precipitation: A 17-year monthly analysis based on gauge observations, satellite estimates, and numerical model outputs. *Bull. Amer. Meteor. Soc*., **78**, 2539-2558.

Zhang, Y. C. W. B. Rossow, A. A. Lacis, V. Oinas, and M.I. Mishchenko, 2004: Calculation of radiative fluxes from the surface to top of atmosphere based on ISCCP and other global data sets: Refinements of the radiative transfer model and the input data. J. Geophys. Res., 109, D19105, doi:10.1029/2003JD004457.

Table 1 Global annual-mean climatological properties of CSU MMF vs observational estimates.

Property	MMF	Observation	Source
TOA Outgoing longwave radiation (W m^{-2})	238.3	234.1	ISCCP-FD
TOA Absorbed Solar Radiation (W m^{-2})	237.6	238.3	ISCCP-FD
Longwave cloud forcing (W m^{-2})	24.5	25.6	ISCCP-FD
Shortwave cloud forcing (W m^{-2})	-52.6	-50.0	ISCCP-FD
Net surface longwave radiation (W m^{-2})	56.2	49.4	ISCCP-FD
Clear-sky net surface longwave radiation (W m^{-2})	83.7	78.7	ISCCP-FD
Net surface shortwave radiation (W m^{-2})	158.8	165.9	ISCCP-FD
Clear-sky surface shortwave radiation (W m^{-2})	216.4	218.6	ISCCP-FD
Precipitation rate (mm day^{-1})	2.80	2.66	CMAP
Precipitable water (mm)	25.2	24.5	NVAP
Latent heat flux (W m^{-2})	81.2	78	KT
Sensible heat flux (W m^{-2})	22.9	24	KT
Total Cloud Amount (%)	67.0	66.7	ISCCP
Low cloud amount (%)	22.9	26.4	ISCCP
Middle cloud amount (%)	17.0	19.1	ISCCP
High cloud amount (%)	27.2	21.3	ISCCP

Figures

Figure 1. Annual mean precipitation in mm day^{-1} for (top) MMF, (middle) CMAP observations, and (bottom) MMF minus CMAP.

Figure 2. Annual mean precipitable water in mm for (top) MMF, (middle) NVAP observations, and (bottom) MMF minus NVAP.

Figure 3. Annual mean longwave cloud effect in W $m^{-2}$for (top) MMF, (middle) ISCCP-FD observational estimates, and (bottom) MMF minus ISCCP-FD.

Figure 4. Annual mean shortwave cloud effect in W $m^{-2}$for (top) MMF, (middle) ISCCP-FD observational estimates, and (bottom) MMF minus ISCCP-FD.

Figure 5. The mean seasonal cycle of precipitation during 1986-2004 as in terms of the average amplitude of the annual harmonic (left top) simulated by the MMF and (left bottom) derived from the CMAP observations. The (right top) simulated and (right bottom) observed month of maximum (phase) of the precipitation annual harmonic.

Figure 6. EOF1 (top) and EOF2 (middle) and the associated principle-component time series (bottom) of bandpass-filtered monthly simulated (left) and observed CMAP (right) precipitation for years 1986-2004.

Figure 7. El Niño minus La Niña yearly anomaly composites of (top) precipitable water, (middle) longwave cloud effect, and (bottom) shortwave cloud effect for (left panels) the MMF simulation, and (right panels) as observed.

Figure 8. The symmetric raw OLR spectral power divided over the background power (signal-to-noise ratio spectrum) as (left) simulated by the MMF, (middle) derived from NOAA daily observations, and (right) simulated by the CAM3. Superimposed are the theoretical shallow-water dispersion curves for the equatorial Rossby and Kelvin waves for the equivalent depths of 12, 25, and 50 m. Contour interval is 0.1 with contours beginning at 1.

Figure 9. The Hovmuller diagram of the OLR anomalies averaged for the latitudes 15^{o}S to 15^{o}N for the 96-day time sample of the MMF diurnal output for the (top left) MJO-filtered band, (top right) Kelvin-wave filtered band, (bottom left) equatorial Rossby-wave band, and (bottom right) unfiltered with the sample-mean removed.

Figure 10. The geographical distribution of the for the MJO-filtered OLR variance averaged for the (top) boreal winter , (middle) summer, and (bottom) annual mean for (left) MMF simulation and (right) NOAA observations.

Figure 11. Same as Fig. 10, but for the Kelvin-wave filtered OLR anomaly.

Figure 12. Time series of the 96-day-averaged MJO-filtered OLR variance for the (top) MMF simulation and (bottom) NOAA observations. The multiyear mean was removed.

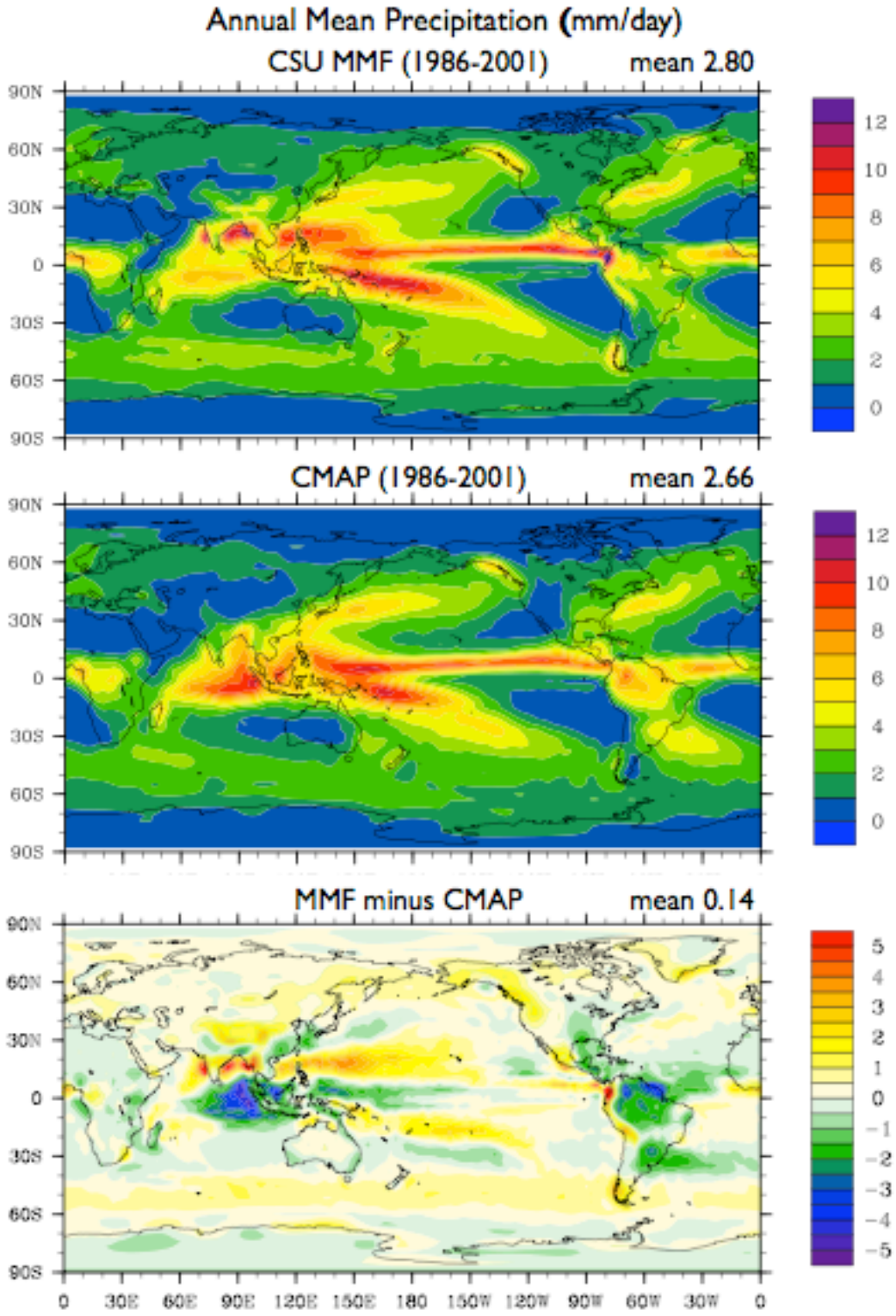

Figure 1. Annual mean precipitation in mm day^{-1} for (top) MMF, (middle) CMAP observations, and (bottom) MMF minus CMAP.

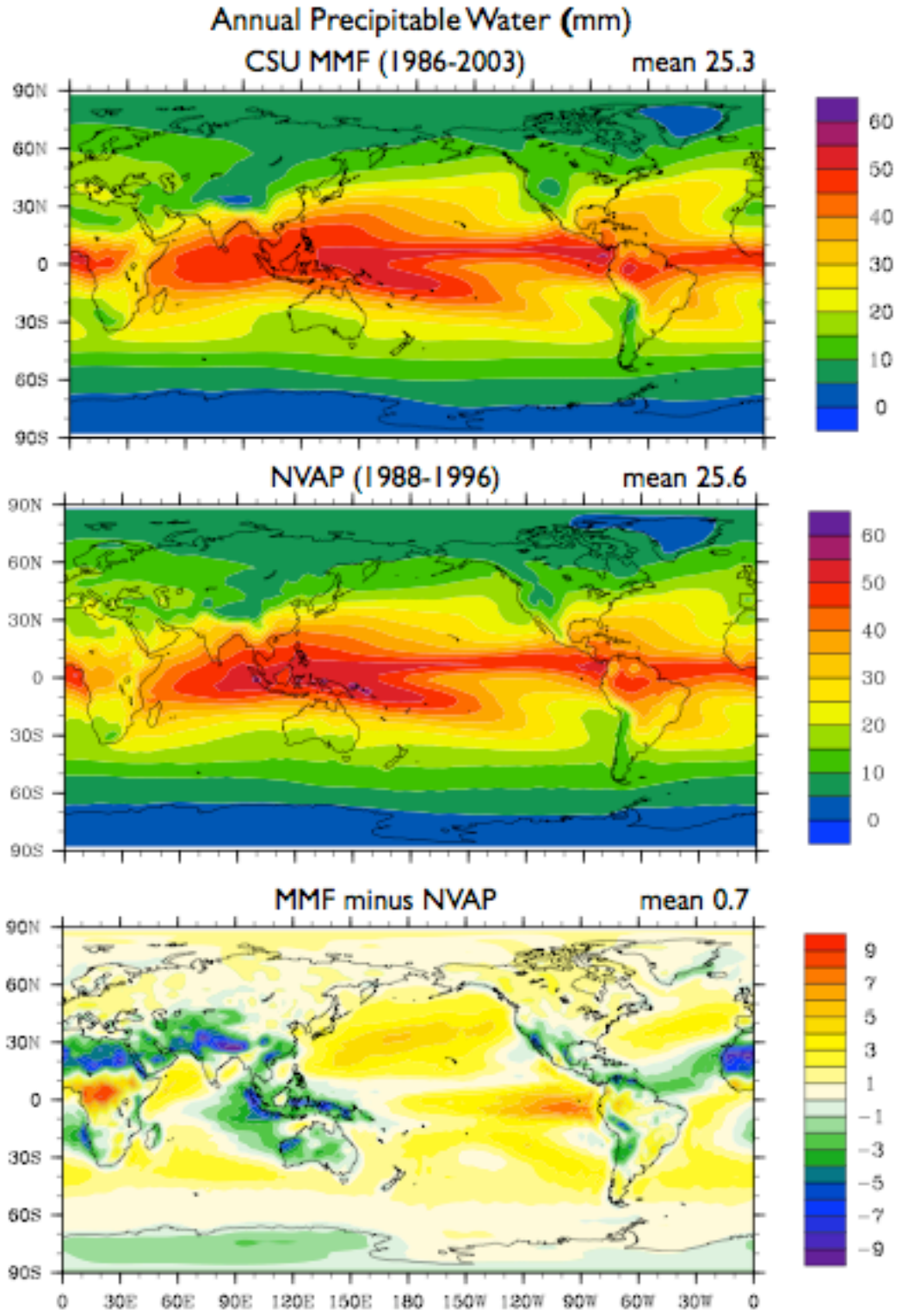

Figure 2. Annual mean precipitable water in mm for (top) MMF, (middle) NVAP observations, and (bottom) MMF minus NVAP.

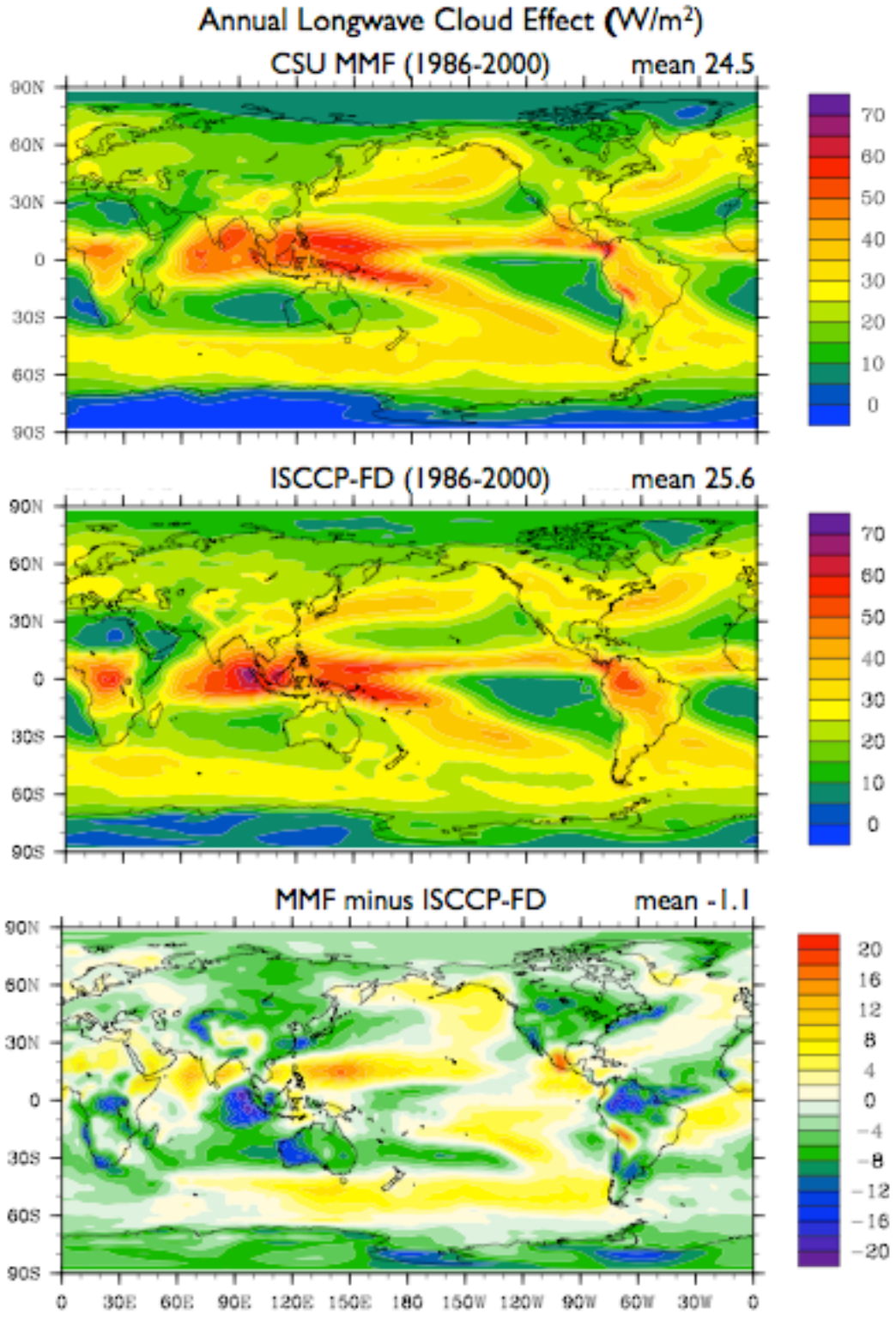

Figure 3. Annual mean longwave cloud effect in W m^{-2} for (top) MMF, (middle) ISCCP-FD observational estimates, and (bottom) MMF minus ISCCP-FD.

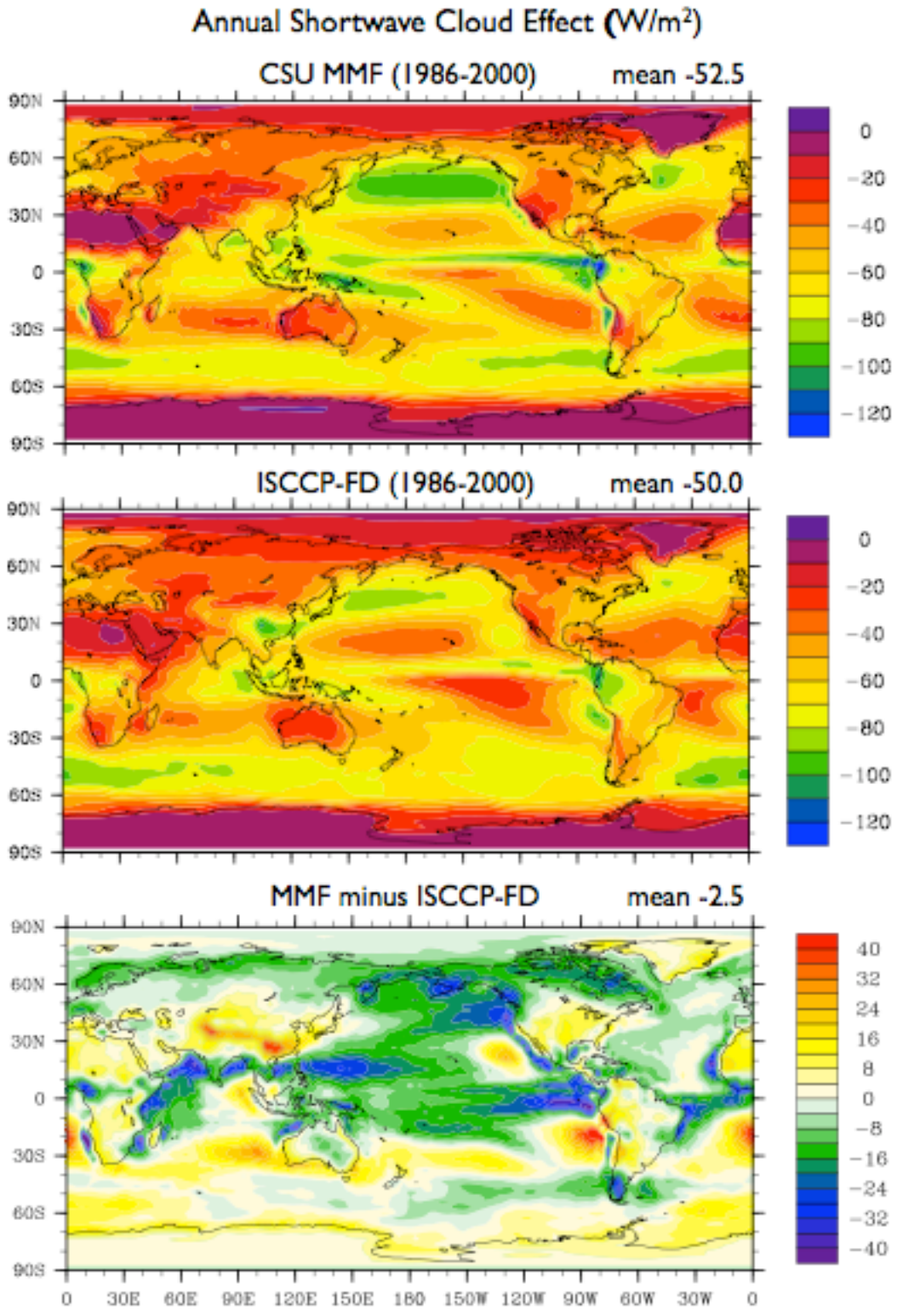

Figure 4. Annual mean shortwave cloud effect in W m^{-2} for (top) MMF, (middle) ISCCP-FD observational estimates, and (bottom) MMF minus ISCCP-FD.

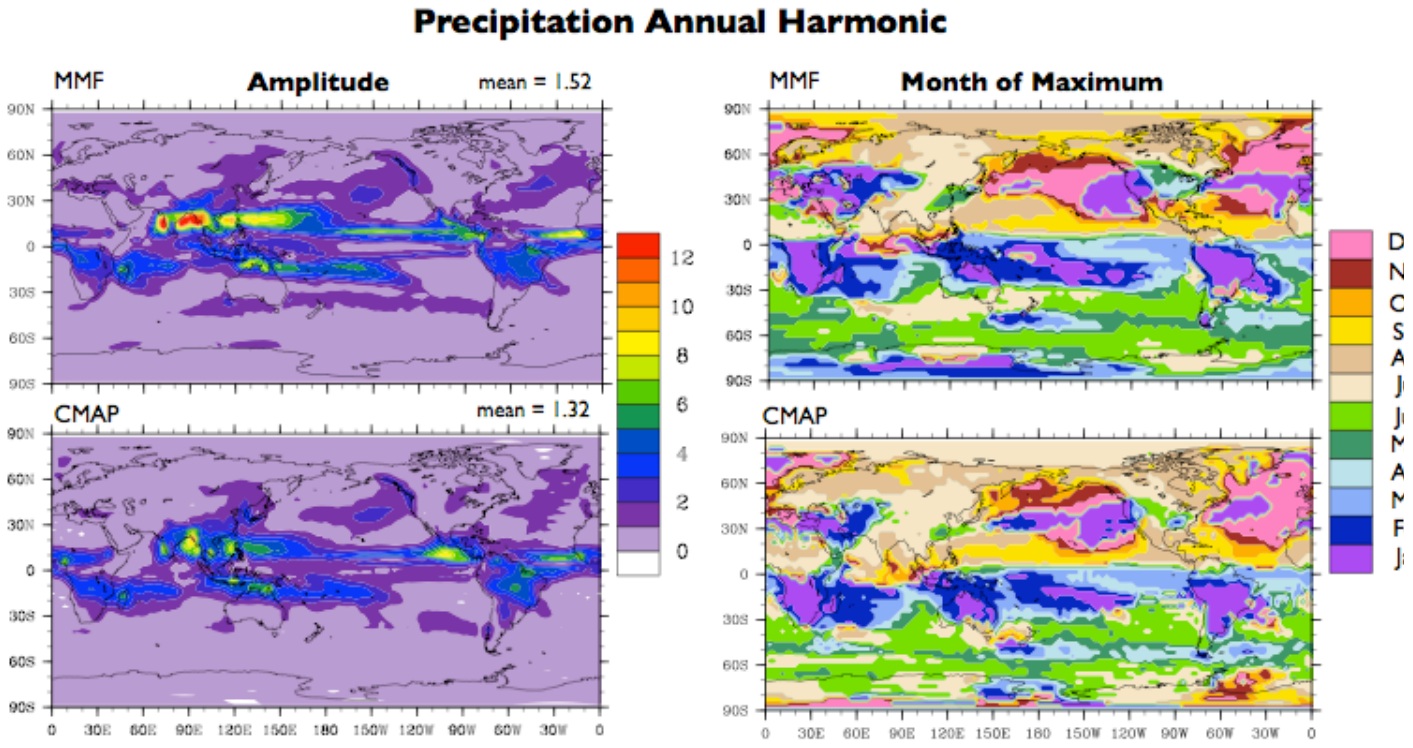

Figure 5. The mean seasonal cycle of precipitation during 1986-2004 as in terms of the average amplitude of the annual harmonic (left top) simulated by the MMF and (left bottom) derived from the CMAP observations. The (right top) simulated and (right bottom) observed month of maximum (phase) of the precipitation annual harmonic.

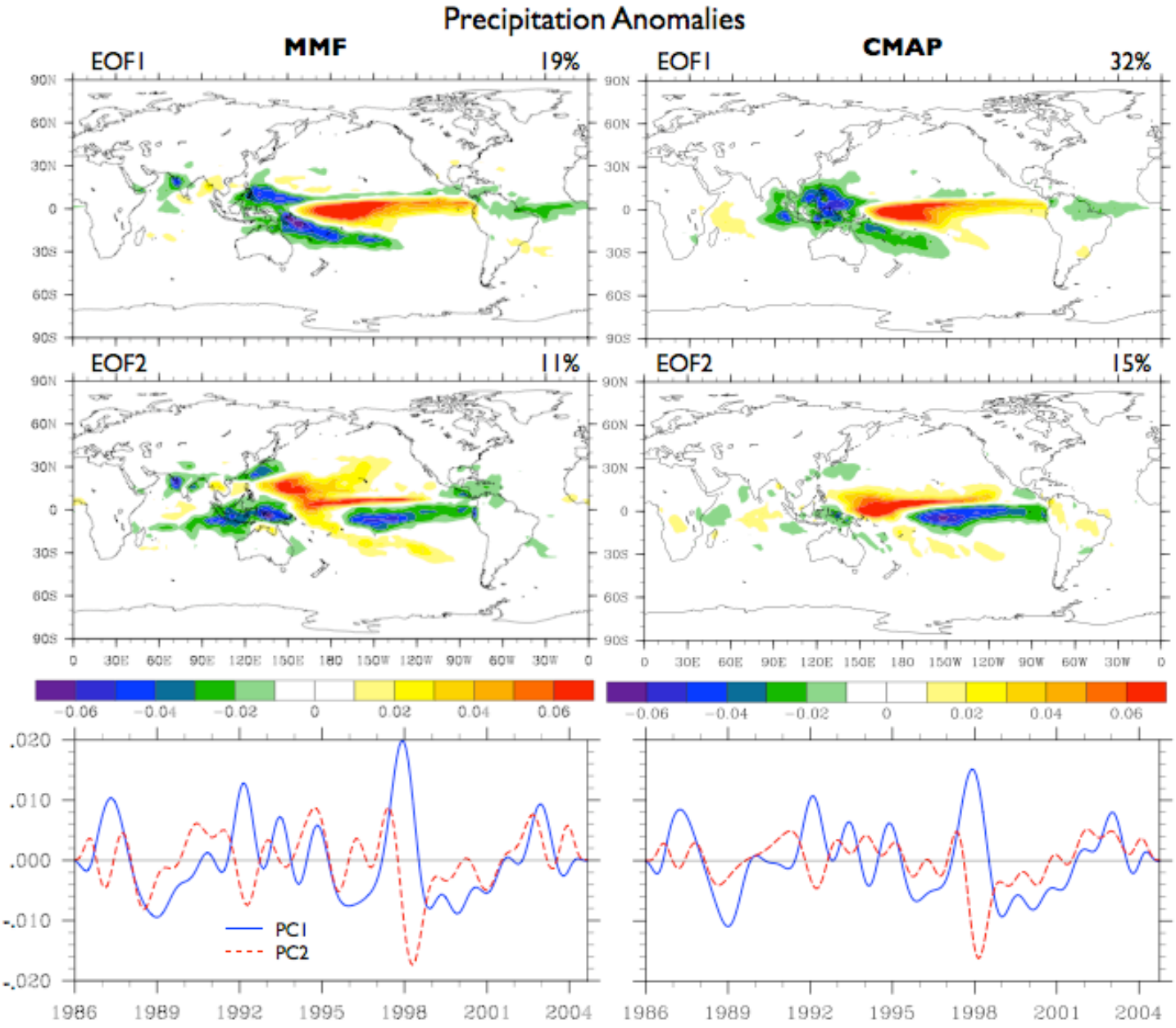

Figure 6. EOF1 (top) and EOF2 (middle) and the associated principle-component time series (bottom) of bandpass-filtered monthly simulated (left) and observed CMAP (right) precipitation for years 1986-2004.

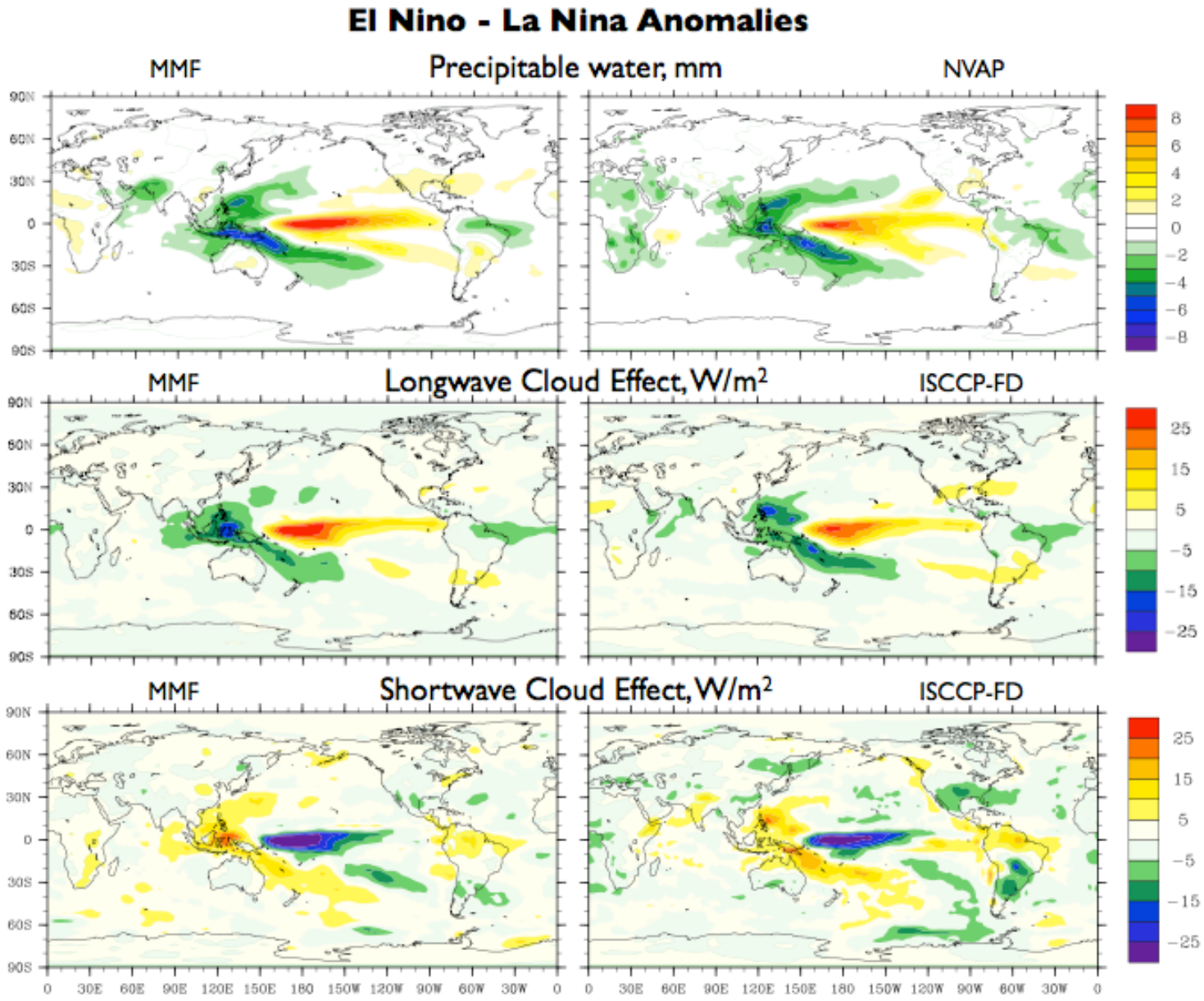

Figure 7. El Niño minus La Niña yearly anomaly composites of (top) precipitable water, (middle) longwave cloud effect, and (bottom) shortwave cloud effect for (left panels) the MMF simulation, and (right panels) as observed.

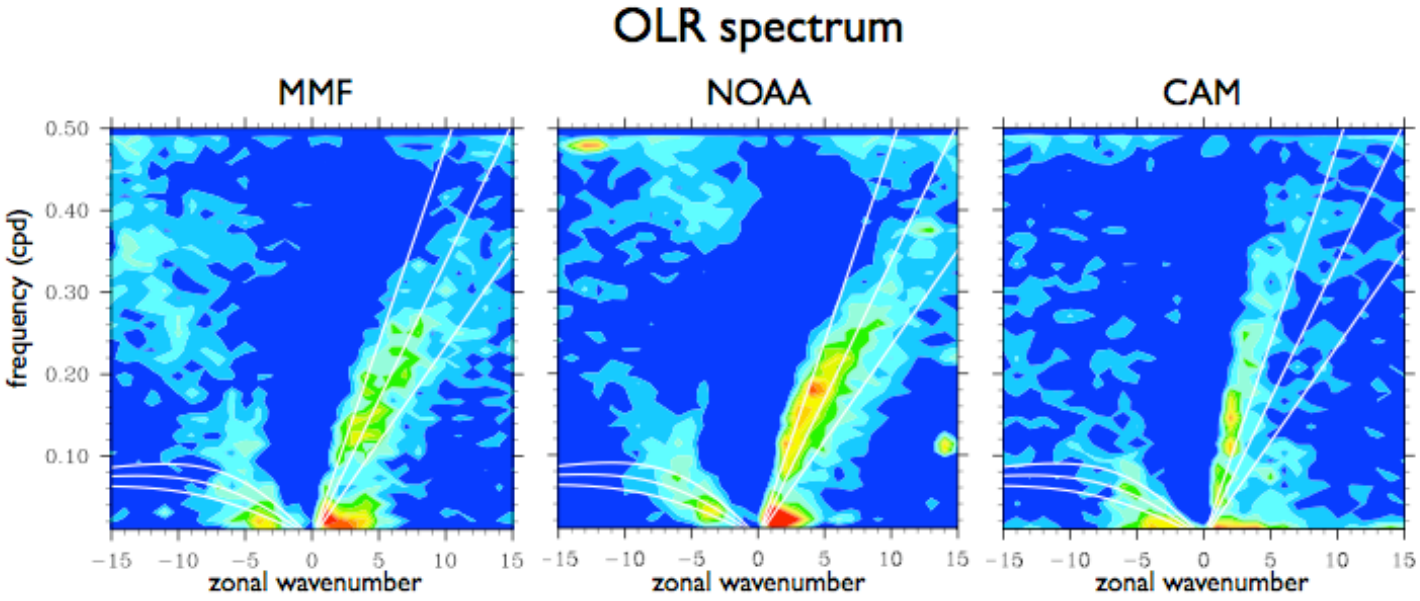

Figure 8. The symmetric raw OLR spectral power divided over the background power (signal-to-noise ratio spectrum) as (left) simulated by the MMF, (middle) derived from NOAA daily observations, and (right) simulated by the CAM3. Superimposed are the theoretical shallow-water dispersion curves for the equatorial Rossby and Kelvin waves for the equivalent depths of 12, 25, and 50 m. Contour interval is 0.1 with contours beginning at 1.

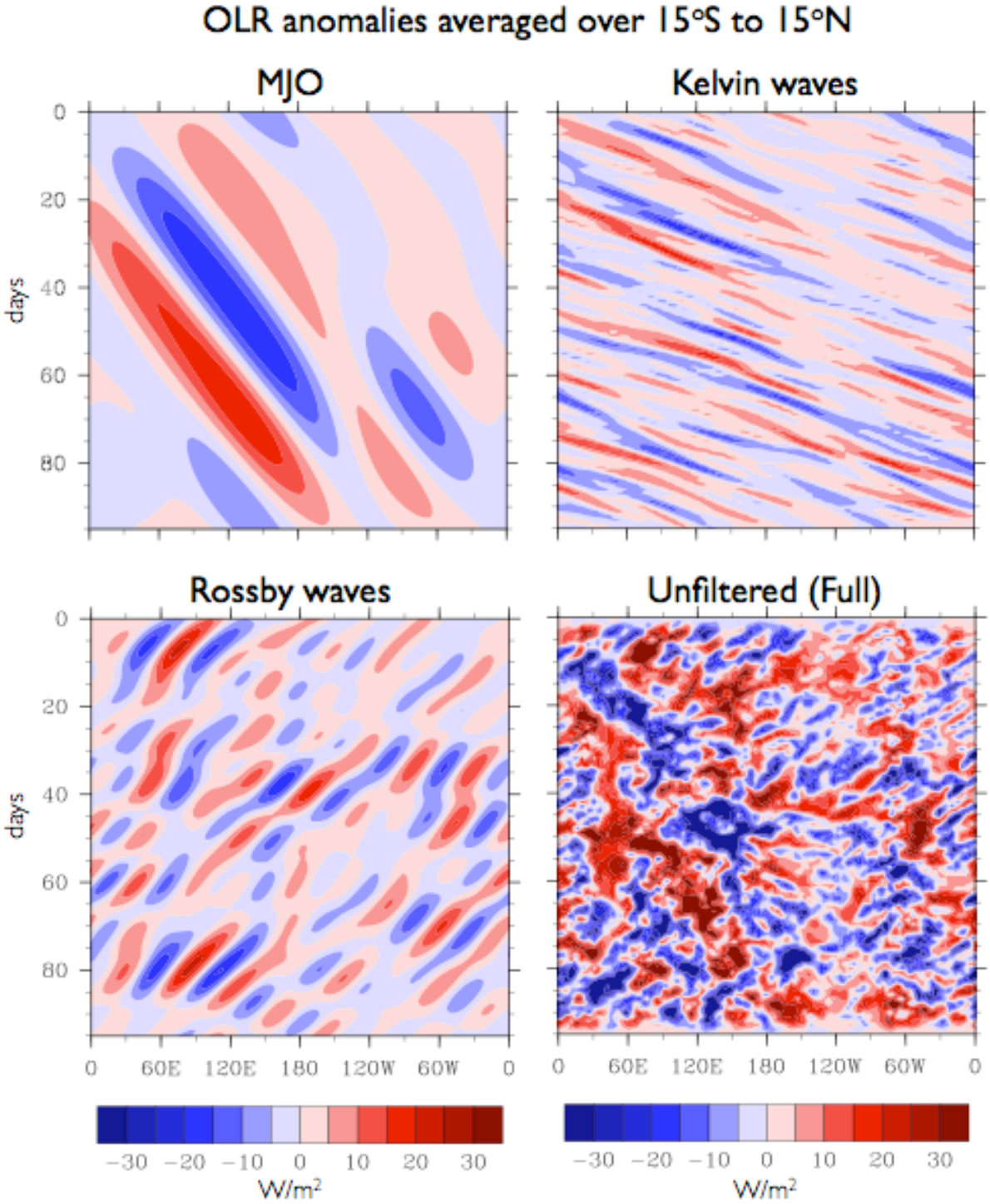

Figure 9. The Hovmuller diagram of the OLR anomalies averaged for the latitudes 15°S to 15°N for the 96-day time sample of the MMF diurnal output for the (top left) MJO-filtered band, (top right) Kelvin-wave filtered band, (bottom left) equatorial Rossby-wave band, and (bottom right) unfiltered with the sample-mean removed.

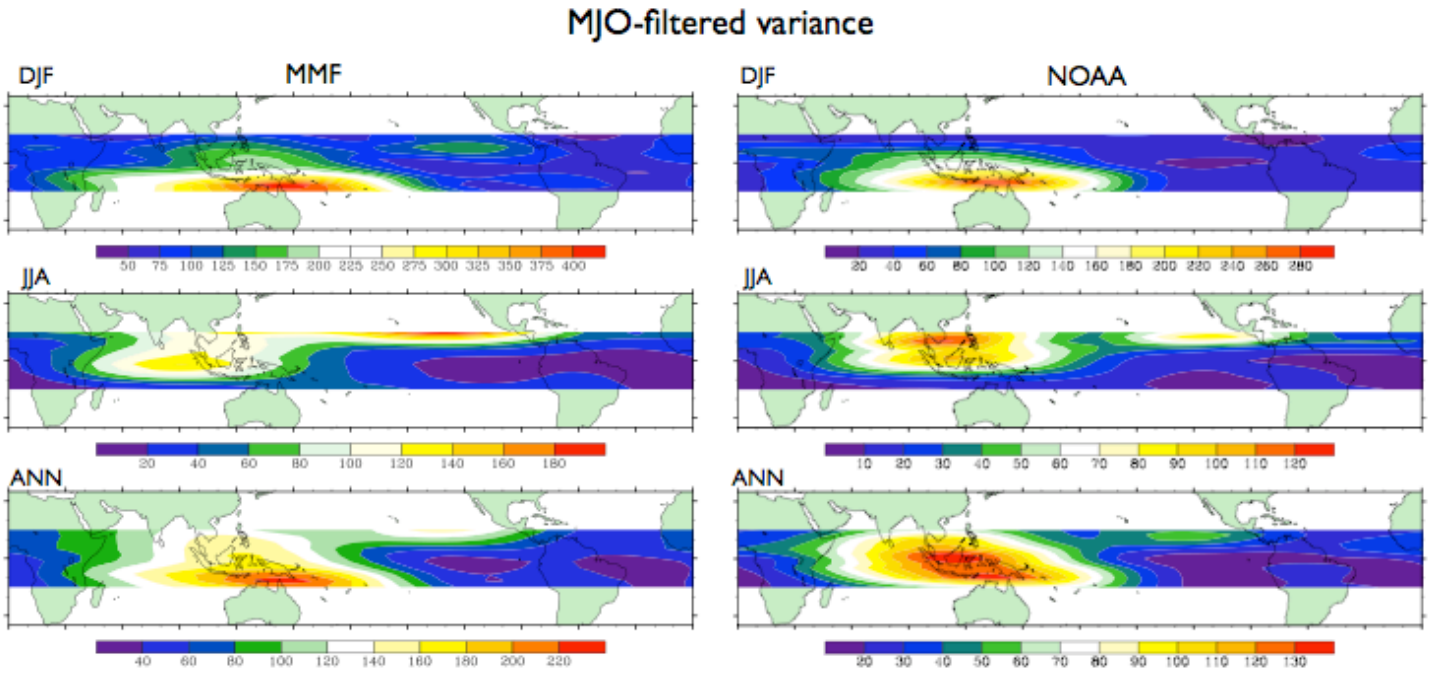

Figure 10. The geographical distribution of the for the MJO-filtered OLR variance averaged for the (top) boreal winter , (middle) summer, and (bottom) annual mean for (left) MMF simulation and (right) NOAA observations.

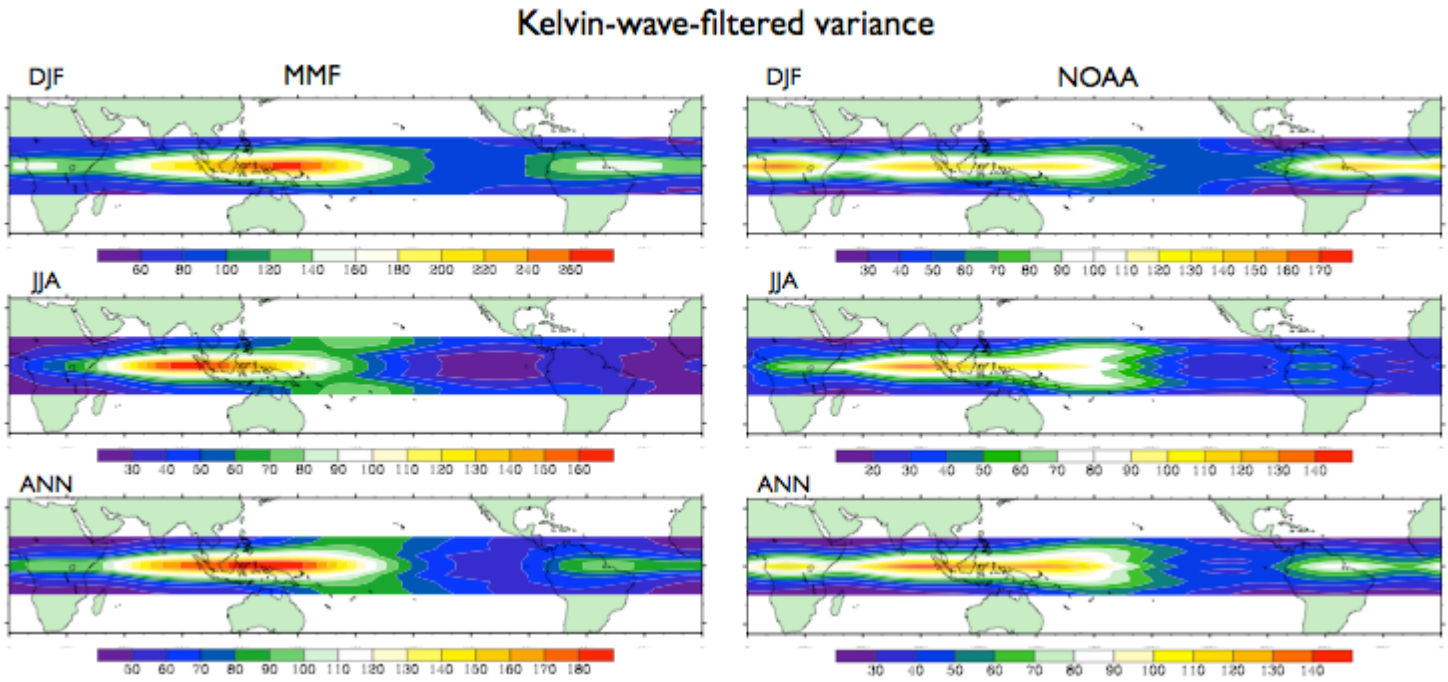

Figure 11. Same as Fig. 10, but for the Kelvin-wave filtered OLR anomaly.

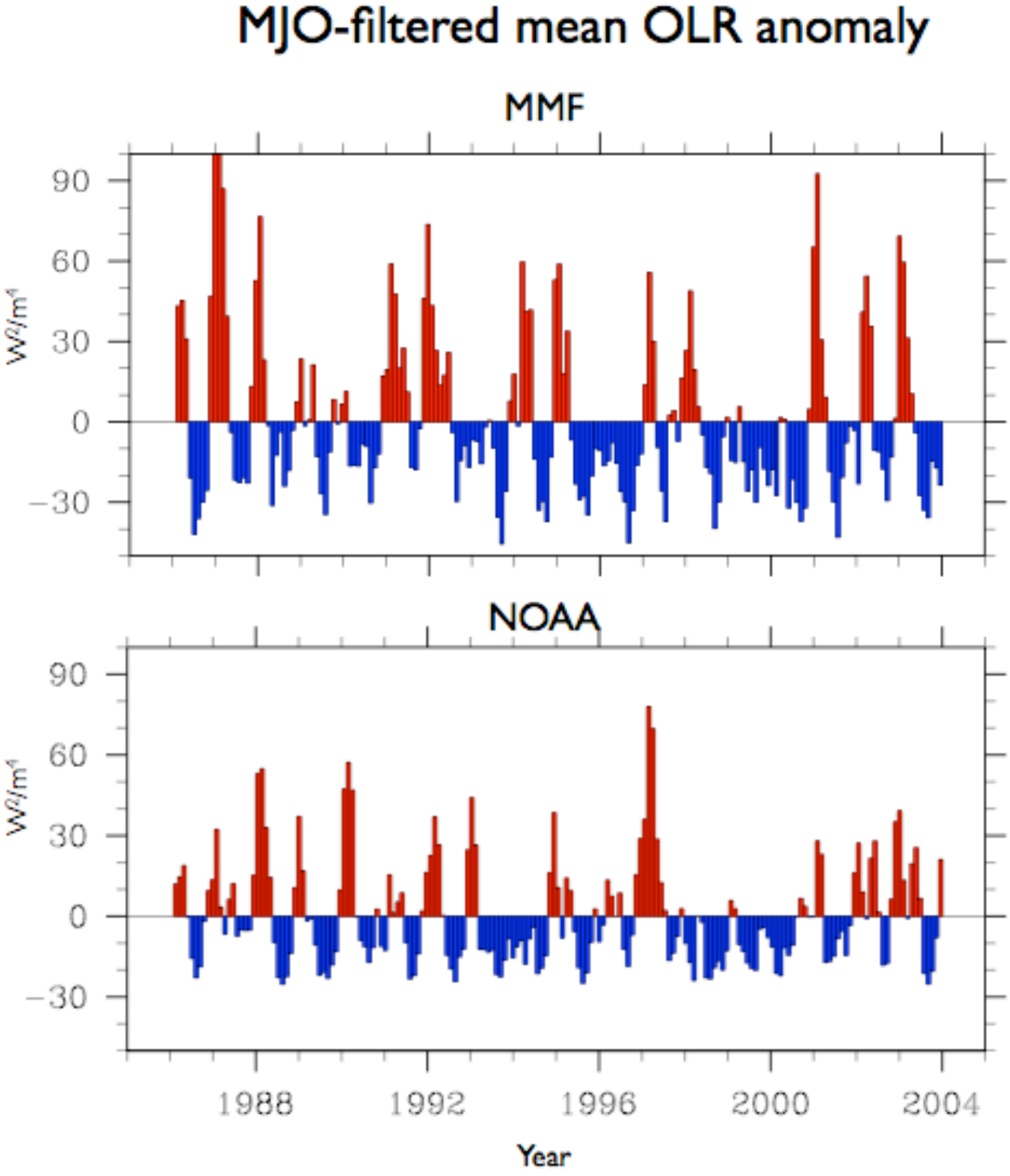

Figure 12. Time series of the 96-day-averaged MJO-filtered OLR variance for the (top) MMF simulation and (bottom) NOAA observations. The multiyear mean was removed.